https://doi.org/10.1016/j.actamat.2022.118294

Graphical Abstract

Local structure in high-entropy transition metal diborides

Mattia Gaboardi, Frederic Monteverde, Federico Saraga, Giuliana Aquilanti, Lun Feng, William Fahrenholtz, Gregory Hilmas

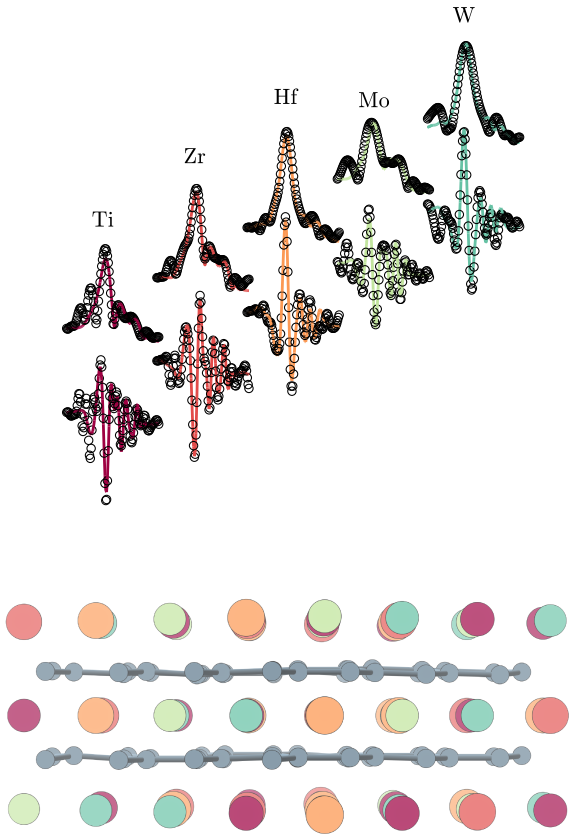

Local structure in high-entropy transition metal diborides

Mattia Gaboardi[a], Frederic Monteverde[b,*], Federico Saraga[b], Giuliana Aquilanti[a], Lun Feng[c], William Fahrenholtz[c], Gregory Hilmas[c]

[a] *Elettra - Sincrotrone Trieste S.C.p.A. S.S. 14 km 163.5 in Area Science Park 34149 Basovizza Trieste Italy.*
[b] *Institute of Science and Technology for Ceramics National Research Council of Italy via Granarolo 64 I-48018 Faenza Italy.*
[c] *Missouri University of Science and Technology Rolla MO 65409 United States.*

Abstract

Studies on high-entropy materials often speculate about the effects of lattice distortion and disorder on characteristics such as hardness, thermal expansion, and electronic properties. Notwithstanding the ongoing race to discover new compositions, investigations of the local structure at the atomic level remain sparse at best. Additionally, assessments of the homogeneity of the distribution of metals within the lattice sites are often restricted to techniques such as energy dispersive spectroscopy which might lead to an inaccurate picture of the bulk material. Herein, we report an extensive and systematic study of a class of emerging high-entropy ceramics that uses a combination of high-resolution synchrotron powder diffraction and extended X-ray absorption fine structure analysis. Our data are consistent with a random distribution of atoms with local strain around the *d*-metals sites, which describes the bulk structure of these materials. Moreover, a linear trend is observed between the average structure and the first-neighbour distances, regardless the number (from 3 to 5) and type (Ti, Zr, Nb, Hf, Ta, Mo, W) of metals that constitute the high-entropy ceramic, which suggests that any description of properties for such materials need to go beyond the simple dichotomy of long-range order and local structure.

Keywords: high-entropy materials, EXAFS, X-ray diffraction
PACS: 0000, 1111

*corresponding author: frederic.monteverde@istec.cnr.it

2000 MSC: 0000, 1111

1. Introduction

High-entropy materials (HEMs) are a class of compounds whose formation is fostered owing to their enhanced molar configurational entropy. Whilst generally exhibiting a high degree of lattice symmetry, widespread chemical disorder is achieved employing multiple elements of similar valence/charge and slightly dissimilar sizes. Since the discovery of HE alloys in 2004 [1, 2, 3, 4, 5], the HEM label has been extended to the most recent ceramic counterparts. However, an important distinction stands between HE alloys and ceramics (*e.g.* oxides, carbides, diborides). While the former are characterized by a relatively simple lattice, often described by a single atomic site occupied by several elements with equal atomic fractions, the latter present two or more sublattices: one for the non-substituted element (*e.g.* O, C, N, and B) and one or more for the metal species, such as group IV-V-VI transition metals (TMs) that are object of the present work. Consequently, only the metal-sublattice is chemically disordered while, at the same time, the remaining anionic sublattice is configurationally ordered. Whether the label "high-entropy" ceramics is appropriate or not to describe these multi-elemental mixtures of borides, carbides, nitrides, or oxides is a matter of open debate. Recently proposed terms "compositionally-complex", "entropy-stabilized", or "HE metal-sublattice" -ceramics seem to be more suitable to address the key feature of higher configurational entropy associated with the mixing of different constituents in only a fraction of the lattice [6, 7, 8]. Having different sizes, the TMs should distort at least one sublattice without, however, disrupting the formation of a crystalline structure. These lattice distortions may lead to unrivalled properties, many of which can be highly beneficial for particular applications.

In this scenario, HE ceramics (HECs) form a wide class of compounds, within the extended family of ultrahigh temperature ceramics (UHTCs), which are proposed for applications ranging from thermal/environmental barriers, catalysts for water splitting [9], and electrodes in lithium-ion batteries [10], in addition to hard- and wear-resistant coatings for nuclear materials in the next generation fusion power plants. In recent years a frantic race has been on to increase the number of HEMs which has led to the synthesis of several novel compounds, while only a limited number of studies have tried

to improve their mechanistic understanding, ranging from the grade of disorder, to internal strain and intrinsic properties [11]. Investigations of the homogeneous distribution of metals in the sublattice sites remain sparse at best, with computational studies suggesting segregation of some species at the grain boundaries, *e.g.* in ZrB_2 [12]. Dai *et al.* predicted only minor lattice distortions in $Ti_{0.2}Zr_{0.2}Hf_{0.2}Nb_{0.2}Ta_{0.2}B_2$ as compared to its carbide counterpart [13] and mainly occurring through the displacement of boron atoms. In a recent study, our group investigated several compositions of 5-elements transition-metal diborides and established a method to combine synchrotron XRPD profile analysis with electron microscopy. We concluded that the microstrain refined by high-resolution diffraction is directly related to chemical fluctuations on the transition metals sublattice [14]. As a result, microstrain can be used as observable to measure the extent of chemical homogeneity in these materials and the obtainment of a genuine solid solution. Rost *et al.* studied the chemical homogeneity at the long- and short-ranges in HE oxides in the purely covalent (Mg,Co,Ni,Cu,Zn)O cubic system employing electron-microscopy, X-ray powder diffraction (XRPD), and extend X-ray absorption fine structure (EXAFS), concluding that distortions occur through disorder in the oxygen sublattice [15, 16]. In this context, the term "entropy-stabilised" was appropriately adopted because the relevant contribution of the configurational entropy to stabilise the five-cation rocksalt type oxide was proven. For the totality of other so-called HECs (including those in the present study), the stabilisation effect of the increased mixing entropy has not yet been established experimentally. Fracchia *et al.* have used pre-edge XAS analysis to study the occupational disorder in the two metal-sublattices of an eight-cation inverse-spinel solid solution [17]. Jiang *et al.* have studied HE chalcogenides conducting high-angle annular dark field (HAADF) and atomic X-ray EDS analysis using scanning transmission electron microscopy (STEM) at different length-scales, demonstrating homogeneous distribution of all elements from the micrometer to nanometer scale [18]. However, despite the macroscopic existence of lattice strains showed by XRD, their type and spatial distributions was found unclear. Atom probe tomography (APT) was used by Chellai *et al.* to investigate HE oxide nano-powders, confirming that the cations are distributed homogeneously at the atomic level [19]. Cheng *et al.*, using high-energy XRD and pair-distribution function (PDF) analysis, showed the existence of lattice distortion in the crystalline framework of $(Ce,La,Pr,Sm,Y)O_2$, revealing an unexpected flexibility in the structure and properties of HE oxides at high-pressure [20]. In this context, studies

on the disorder of HE diborides are still at an early stage. After the first report in 2016 by Gild *et al.*, who showed a strategy to synthesize several 5-elements HE-diborides with single-phase hexagonal AlB_2-type lattice [21]; other investigations have typically focused on the synthesis and optimization of new compositions and the assessment of their mechanical properties [22, 23, 24, 25, 26], while fundamental studies have been limited to the understanding of defects [27].
To fill this gap in knowledge, we designed an extensive and systematic experimental campaign using high-resolution synchrotron-radiation XRPD and EXAFS analysis to combine the study of the long-range structure with additional insights into the local order and chemical environment on HE-UHTCs. Our analysis disclosed the random distribution of metals with local strain of the boron atoms around the *d*-metals.

2. Methods

A palette of 9 different combinations with 3, 4, or 5 coexisting TMs was selected to produce a diverse collection of compositions. All samples were designed to have both Zr and Ti owing to their established affinity in forming homogeneous solid solutions and to allow the continuous comparison between one large and one small *d*-metal across the entire series. Combinations having both Hf and Ta in the same starting compositions were intentionally avoided due to superposition of XAFS spectra with similar absorption edges. The complete set of synthesized samples is summarized in Table 1.

Synthesis of samples

Hafnium oxide (HfO_2, 99% , -325 mesh; Alfa Aesar), zirconium oxide (ZrO_2, 99%, SC101, mean size 0.8 μm, MEL Chemicals), titanium oxide (TiO_2, 99.9%, P25, mean size 20 nm, Degussa), tantalum oxide (Ta_2O_5, 99.85%, - 325 mesh, Alfa Aesar), niobium oxide (Nb_2O_5, 99.9%, - 325 mesh, Sigma-Aldrich), molybdenum oxide (MoO_3, 99.9%, 6 μm, US Research Nanomaterials, Houston, TX), tungsten oxide (WO_3, 99.9%, $\sim$80 nm, Inframat Advanced Materials, Manchester, CT), carbon black (C, BP120, 30 m^2/g, Cabot), and boron carbide (B_4C, purity 96.8%, 0.6 $\sim$1.2 μm, H.C. Starck) were used as starting materials. Purity and particle sizes are from the producers' datasheets. Different compositions (*cfr.* Table 1) were designed using different metal (Me) oxides to produce single-phase DSS powders, according

Table 1: List of designed combinations used to synthesize the diboride solid-solution (DSS) powders. Investigated X-ray absorption edges and energies (E_0) are also reported at the bottom.

	molar composition in M-B_2						
ID	Ti	Zr	Hf	Ta	Nb	Mo	W
X-1	1/3	1/3	1/3	-	-	-	-
X-2	1/3	1/3	-	1/3	-	-	-
X-3	1/4	1/4	1/4	-	1/4	-	-
X-4	1/4	1/4	-	1/4	1/4	-	-
X-5	1/4	1/4	-	1/4	-	1/4	-
X-6	1/4	1/4	1/4	-	-	-	1/4
X-7	1/5	1/5	1/5	-	1/5	1/5	-
X-8	1/5	1/5	1/5	-	-	1/5	1/5
X-9	1/5	1/5	-	1/5	1/5	1/5	-
edge	K	K	L_3	L_3	K	K	L_3
E_0 (eV)	4996	17998	9561	9881	18986	20000	10207

to reactions 1-3:

$$MO_2 + \frac{1}{2}\,B_4C + \frac{3}{2}\,C \longrightarrow MeB_2 + 2\,CO\,(g) \quad [M{=}Ti, Zr, Hf] \tag{1}$$

$$\frac{1}{2}\,M_2O_5 + \frac{1}{2}\,B_4C + 2\,C \longrightarrow MB_2 + \frac{5}{2}\,CO\,(g) \quad [M{=}Ta, Nb] \tag{2}$$

$$MO_3 + \frac{1}{2}\,B_4C + \frac{5}{2}\,C \longrightarrow MB_2 + 3\,CO\,(g) \quad [M{=}W, Mo] \tag{3}$$

The designed combinations of metal oxides were weighed to obtain equiatomic amount of TMs in the final DSS powders. Carbon black (C) was added in stoichiometric amounts according to reactions 1-3, while about 13 wt% excess B_4C was added to all batches to compensate for loss of B during synthesis [28]. The raw powders of the starting metal oxides mixtures were homogenized with the reducing agents $B_4C + C$ (necessary for the boro-carbothermal reduction reaction) using a high-energy planetary mill (HEPM, Fritsch Pulverisette 6 - Germany) with anhydrous ethyl alcohol as the solvent. The milling jar and milling balls (3 mm diameter) were Y-stabilized zirconia. The milling cycle consisted of six 15 min-steps at 400 rpm alternated with five 10 min-breaks of cooling, thus bringing the total processing time to 90

min. After milling, the mixtures were dried overnight in a ventilated oven at 343 K and then sieved (150 μm mesh size). The synthesis of the single-phase DSS powders was conducted in two separate thermal cycles. The first cycle consisted in the boro-carbo thermal reduction (BCTR): pellets (20 mm diameter and about 2 g) for each unreacted X-n starting mixture listed in Table 1 were obtained using a uniaxial press and applying a pressure up to 3.5 MPa, followed by a cold isostatic pressing up to 200 MPa. Prior to BCTR, the pellets were first housed in closed graphite-paper boxes which, in turn, were placed inside a lid-free graphite-crucible. The boxes were randomly pierced to allow for volatile products of the BCTR to be pumped away. BCTR was conducted in a special high temperature furnace (LHTG 200-300/24-1G, Carbolite Gero, Germany) under dynamic vacuum ($\sim$30-70 Pa). The temperature was raised to 1973 K with a heating rate of about 70 K/min and isothermally held for 120 min. The as-treated products were pulverized using Y-stabilized zirconia mortar and pestle and sieved using a 250 μm mesh size grid, and then re-pressed in a pellet shape. The second and final thermal cycle was conducted in the same special furnace under dynamic vacuum. The temperature is raised to 2373 K with a heating rate of about 70 K/min and isothermally held for 60 min. Then, similarly to the first cycle, the furnace is let to cool down naturally. For the X-8 composition, a second thermal step was performed using a spark plasma sintering (SPS) furnace and applying a pressure up to 50 MPa (more details are reported in the Supporting Information). A field emission scanning electron microscope (FESEM, ZEISS Σigma – Germany) equipped with an energy dispersive spectroscopy (EDS) detector (INCA Energy 300, Oxford Instruments - UK) was used to screen the chemical composition of the obtained specimens. A part of each heat-treated X-n pellet was pulverized for subsequent structural analysis.

Structural analysis

Synchrotron radiation XRPD data were collected in Debye-Scherrer geometry on the high-resolution MCX beamline at the Elettra synchrotron light-source (Trieste, Italy) for λ=0.7293 Å (17 keV). A borosilicate capillary (0.3 mm diameter) was filled with sample powder and the diffraction pattern was acquired at room temperature on the 4-circle Huber goniometer by spinning the capillary at 300 rpm. Patterns were then analyzed by means of either Rietveld or Le Bail refinement assuming the AlB_2-type structural model (space group *P6/mmm*) in order to extract the lattice parameters. The instrument profile (typically Gaussian for this beamline) was calculated

using a silicon standard (NIST SRM 640c) by refining the peaks shape with the pseudo-Voigt (PV) function available in the GSAS-II suite [29]. Profile extra-broadening (from the sample) was evaluated using the uniaxial approximation for microstrain and crystalline domain size. K-edge and L_3-edge (*cfr.* Table 1) XAS spectra were collected, at room temperature, on the XAFS beamline at Elettra [30]. A monochromatic beam was obtained using the double silicon crystal monochromator. The Si-111 reflection was employed for the lower energy range (*i.e.* Ti, Ta, Hf, W), whilst the 311 reflection was used for Nb, Zr, and Mo. The spectra were recorded in transmission mode, at room temperature, on pellettized specimens (13 mm diameter) composed by weighted mixtures of boron nitride and finely powdered sample, in order to obtain suitable absorption amplitude. The energy calibration for all samples was attained by simultaneously recording a reference spectra of either a metallic foil or an oxide pellet, depending on the investigated element. Spectra of ZrB_2, TaB_2, HfB_2, and TiB_2 were also collected as reference. Subsequent data processing and analysis was performed using the Demeter suite of programs [31]. From two to three spectra were collected per each edge of each samples to increase the signal to noise ratio. The spectra were aligned, merged and normalized using the program Athena [31]. A suitable atomic background was used above the absorption edge to extract the EXAFS signal. The latter was Fourier transformed using a sine-window in a k-range variable within 2-18 $Å^{-1}$ (depending on the edge and quality of the data). For more details about the refinement of the EXAFS data see Appendix A. Summarizing, first the XRPD data were analysed in order to confirm that the samples were single phase and the patterns refined to obtain the initial model for the subsequent EXAFS analysis. Hence, for each X-n composition, XAFS data were fitted globally (*i.e.* using a multiedge approach) starting from the XRPD refined model and using all the available spectra.

3. Results and Discussion

Fig. 1 shows the Rietveld refined data of sample X-1. Remaining samples are reported in the Supporting Information (see Fig. S-1-S-8). For all samples the most intense peaks are indexed to the space group *P6/mmm*. The only exception relevant to note is given by sample X-6 (*cfr.* Fig. S-5), where a W_2B_5-type impurity phase (s.g. $P6_3/mmc$) was refined with content of 4% (more information about this inclusion are given in the Supporting Information), however its effect on the EXAFS spectra was considered negligible

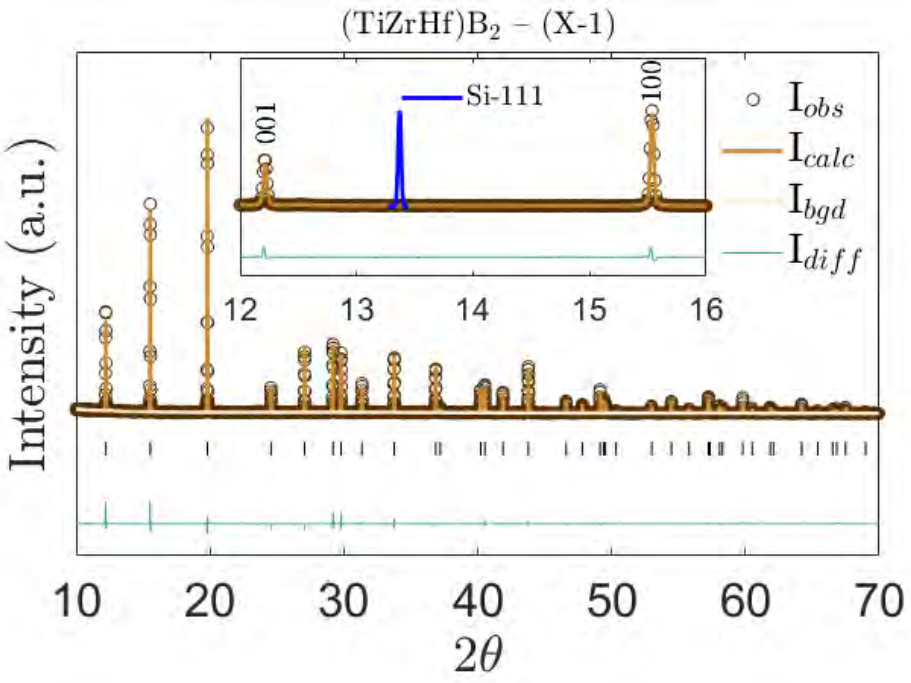

Figure 1: High-resolution synchrotron XRPD pattern and Rietveld refinement of DSS X-1. Inset: magnification on the 001 and 100 perpendicular reflections, showing no apparent broadening compared to the instrumental resolution (Si-111 reflection displayed in blue).

at this level of detail. A simple comparison between these patterns and the silicon standard does not show apparent peak broadening. Detailed profile analysis highlighted negligible domain size-broadening, whilst a small microstrain broadening can be observed in some of the compositions, yet fairly small if compared to previously reported values, obtained with the same level of resolution [24, 32]. Samples X-4 and X-5 had a slight asymmetry in the profile and were Le Bail-refined with two phases with quasi-identical lattice parameters. However, for the sake of simplicity, they will be hereafter considered as single phases. The obtainment of genuine single phases with negligible microstrain broadening is indicative of a great extent of homogenisation in these DSS powders (see also Monteverde *et al.* [14]), with a high level of structural order, at least for the *d*-metals sublattice, which accounts for most of the scattered intensity. The full list of refined structural and microstrain parameters is reported in Table S1. In the *P6/mmm* unit cell, the two sublattices are determined by the chemically disordered TMs, randomly

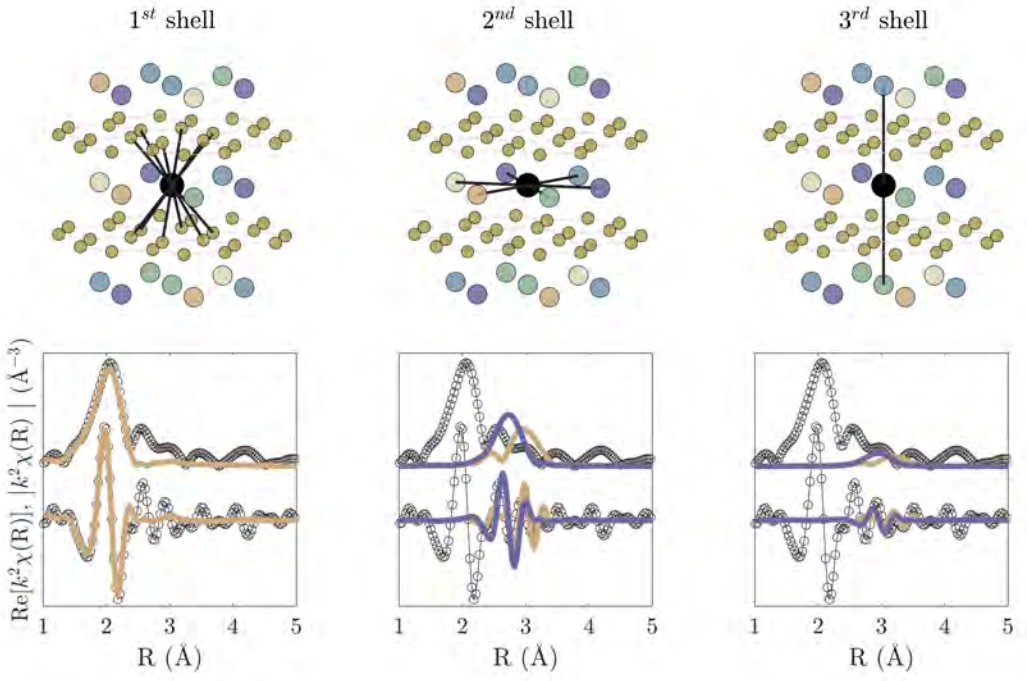

Figure 2: Visual representation of the first three coordination shells (top) from the perspective of the central d-metal (black sphere) in a quaternary random diboride. Below each figure are real data (magnitude and real component, black symbols) for one sample superimposed to modelled components (solid lines) simulating the effect of an L_3- and K-edge central ions (respectively orange and blue solid lines).

occupying the *1a* Wyckoff position in (000), and by the boron atoms, located at the *2d* $(\frac{1}{3}\frac{2}{3}\frac{1}{2})$ sites. The B-sp^2 orbitals form strong σ-type bonds on the (002) planes, while a mixture of ionic and π-covalent bonds characterizes the weaker TM-B interaction [33]. As a consequence, one would expect that the coexistence of several distinct metals on the same lattice sites would generate some internal strain in the structure, which should be accommodated more easily through the deformation of the M-B or M-M bonds, rather than by distorting the (supposedly-rigid) 2D sp^2 covalent boron layers. Fig. 2 (top panels) shows the structure of a generic quaternary diboride, displaying the first three nearest-neighbour shells with respect to the central metal. Considering a single d-metal in the *1a* site as central atom, the first neighbours are the 12 equidistant boron atoms (r_1-distance), to which the metal itself

is coordinated. The B-atoms form two hexagonal rings (one from the above 2D plane and one from below). The second shell is characterized by 6 random TMs (r_2); while the third shell involves two equivalent TMs aligned respectively to the top and bottom layers (r_3).

Table 2: Summary of first-shell distances ($r_{1,i}$) as refined from XRPD (*i.e.* $\langle r_1 \rangle$) and EXAFS analysis (errors between parentheses).

		XRPD	XAFS						
ID	composition	$\langle r_1 \rangle_{xrd}$	Ti−B	Zr−B	Hf−B	Nb−B	Mo−B	Ta−B	W−B
X-1	TiZrHf	2.486	2.46(01)	2.50(01)	2.49(01)	-	-	-	-
X-2	TiZrTa	2.453	2.43(02)	2.47(01)	-	-	-	2.44(01)	-
X-3	TiZrHfNb	2.474	2.46(01)	2.50(01)	2.47(01)	2.48(01)	-	-	-
X-4	TiZrTaNb	2.45	2.43(01)	2.47(01)	-	2.45(01)	-	2.45(01)	-
X-5	TiZrTaMo	2.439	2.43(01)	2.47(01)	-	-	2.44(01)	2.43(01)	-
X-6	TiZrHfW	2.469	2.45(02)	2.49(01)	2.47(01)	-	-	-	2.43(01)
X-7	TiZrHfNbMo	2.462	2.45(02)	2.48(01)	2.46(01)	2.46(01)	2.47(01)	-	-
X-8	TiZrHfMoW	2.442	2.43(02)	2.48(01)	2.45(01)	-	2.43(02)	-	2.40(01)
X-9	TiZrTaNbMo	2.437	2.40(03)	2.46(02)	-	2.44(01)	2.44(02)	2.43(02)	-

A direct observation at the normalized X-ray absorption profiles in the near-edge (XANES) region (*cfr.*Fig. S-9) does not reveal substantial shift for the same metals in different compounds, suggesting that the oxidation state is constantly maintained for all metals, regardless the composition. EXAFS data fitting was used to determine the local structural parameters around the metals (see Appendix A for an exhaustive description). Simulated partial spectra for the first (left), second (middle), and third shells (right) are displayed for reference in Fig. 2 (bottom panels). Each shell produces a well defined partial signal in the EXAFS spectra, which depends not only on the particular shell but also on the edge-type of the metals forming that particular scattering-path, as shown, in different colours, for K- and L_3-contributions to the EXAFS spectra. While a single-shell approach was initially attempted to model the 1^{st} shell, it was soon abandoned due to the partial convolutions occurring between the first three shells, which increases the error. These overlaps generated several challenges in the fitting procedure when more than one transition metal coexisted in the same lattice site. In particular, the 2^{nd} shell should be taken into account in order to optimize the fitting of the 1^{st} shell, while the incorporation of the 3^{rd} shell also improves the fitting of the 2^{nd} one. To this end, for each shell the path degeneracy (N) was replaced to the

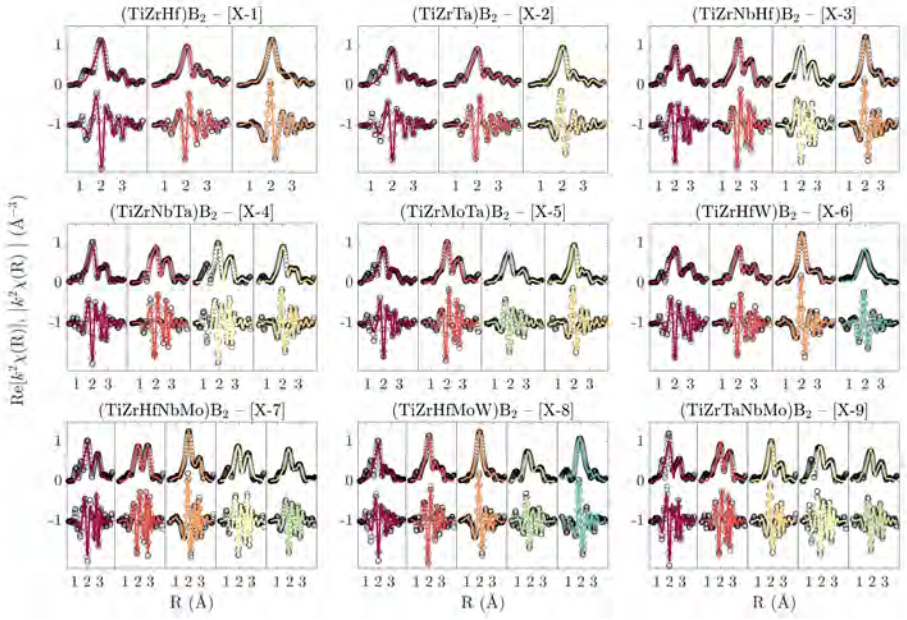

Figure 3: EXAFS spectra (black symbols), reported as $k^2\chi(R)$ for all investigated compositions, with the same order of appearance of the metals displayed in the chemical equation above and global fits (solid lines) reported using similar colour for the equivalent metal. The real components are arbitrarily shifted by -1 below the module.

effective value N_e=N_i/n; with N_i the i-shell path degeneracy and n the number of metals composing the HE-DSS. At the same time, for each composition all spectra at any d-metal edge were simultaneously refined in order to use all the available information from complementary data-sets related to the same chemical mixture. For this reason, second- and third-shell parameters were cross-related on different spectra (*e.g.* for a fixed X-n composition, r_2(TiZr) is refined to be the same in both Ti-XAFS and Zr-XAFS spectra). Fig. 3 shows the global fitting results for the complete set of samples. For each of the spectra, the fitted absorption edge, E_0, remained within ΔE_0=±10 eV, with values consistently similar for the same metals. Table 2 reports the first-shell distances obtained from the global fitting, compared to the values calculated from the XRPD refinements. The EXAFS r_1 fitted values are evenly distributed around the average refined parameter obtained via XRPD (see also Fig. 6). However, r_1 was different for each metal, highlighting local strain, presumably due to the different sizes of the metals. To better visualize

the effect of the local strain, Fig. 4 displays r_1 as plotted against the XRPD refined values. Overall, each metal follows a linear trend with the average lattice parameters, which indicates that the local structure of one metal is affected by the choices of the other metals and the resulting average structure. By assuming r_1 as the sum of the metallic radius of the central *d*-atom and the covalent radius of boron and taking into account the lattice spacings of the pure MB_2 compositions, the 1^{st}-neighbour distances were tentatively ranked as follows: $r_{1,W} \approx r_{1,Mo} < r_{1,Ti} \approx r_{1,Ta} \approx r_{1,Nb} < r_{1,Hf} \approx r_{1,Zr}$, a figure that is consistent with the data. Moreover, a clear trend can be observed by comparing the two ubiquitous metals, Ti and Zr. The average variation calculated from the difference in the r_1-values of these two metals, *i.e.* $r_{1,Zr}$-$r_{1,Ti}$, is 0.044(8) Å and is consistent across all compositions, notwithstanding the linear increase with the lattice volume. In contrast, a maximum difference of about 0.07 Å was measured when both Zr and W (the largest and smallest metals in this study) were present at the same time, suggesting that the highest level of internal strain might be achieved for these compositions. As for the remaining metals (Hf, Nb, Mo, and Ta), they had less strained 1^{st} shells, with r_1 values close to the average refined parameters.

A further correlation between Ti and Zr atoms becomes apparent after considering the relative displacement for r_1 , expressed as

$$\epsilon_i = \frac{\sqrt{|r_{1,i}^2 - \langle r_1 \rangle_{xrd}^2|}}{\langle r_1 \rangle_{xrd}}, \qquad i = (\mathrm{Ti}, \mathrm{Zr}) \tag{4}$$

where $r_{1,i}$ is the XAFS value fitted for M_i-B (M_i=Ti or Zr) and $\langle r_1 \rangle_{xrd}$ is the average XRPD-refined parameter for that specific composition. Fig. 5 show a regular trend occurring between ϵ_{Ti} and ϵ_{Zr} which stops obeying a linear law when the composition of the system incorporates more than four distinct TMs. To give additional indication of the internal strain, we calculated a "strain-free" (sf) displacement, defined as

$$\epsilon_i{}^{sf} = \frac{\sqrt{|r_{1,i}^2 - (r_{1,i}^{sf})^2|}}{r_{1,i}^{sf}}, \qquad i = (\mathrm{Ti}, \mathrm{Zr}) \tag{5}$$

which measures the magnitude of the M_i-B bond-length variation in the as-synthesized DSS compared to the value measured for the single-element diboride.

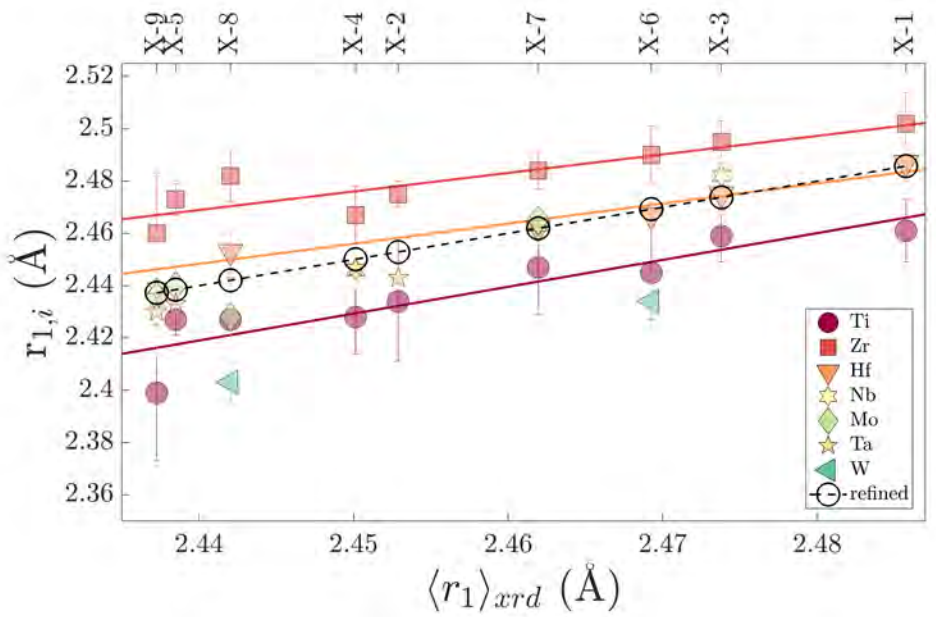

Figure 4: EXAFS first-shell globally fitted distances (r_1) reported as compared to the average distance refined by XRPD. The average distance is also reported (dashed line with crosses) for comparison. Solid lines are a linear fit to the data for $r_{1,\mathrm{Ti}}$, $r_{1,\mathrm{Zr}}$, and $r_{1,\mathrm{Hf}}$.

An average "strain-free" value of r_1 (hereafter $\langle r_1^{sf} \rangle$) can also be calculated for the relative DSS composition using the rule-of-mixture from the tabulated lattice parameters of the single-element diborides (*cfr.* Table S-VI and [34, 35, 36]). Fig. 6 reports the average XAFS-calculated value of r_1 (*i.e.* $\langle r_1 \rangle_{xafs}$) with XRD-refined and "strain-free" values, both showing a linear trend. The contributions of ϵ_{Ti}^{sf} and ϵ_{Zr}^{sf} were summed up and normalized to $\Sigma_i \epsilon_i^{sf}$ in order to plot the relative strain contribution originating from Ti and Zr versus the increasing complexity of the composition (see chart in Fig. 7(a) and paragraph 3.1).

2^{nd} shell distortions (*i.e.* relative to the in-plane M-M distances) are significantly less accurate due to the high level of correlation occurring between so many parameters in a relatively small range of distances. Moreover, 2^{nd} and 3^{rd} shells values should be more sensitive to chemical inhomogeneities, although these were initially dismissed for these samples by assessing negligible levels of microstrain. However, overall deviations of r_2 from the average refined values appear to be smaller compared to r_1 (*cfr.* Table S-II-S-III). This result is in line with smaller equatorial microstrain values, typically half or less than the axial ones (see Table S-I). The smaller equatorial microstrain should be expected for the layered AlB_2 structure where the strongest sp^2 B-B covalent bonds have more influence on the in-plane spacing of metals better than the weaker M-M bonds. The calculated mean variation of r_2 for Ti-Zr gives an average value of 0.02(1) Å. At the same time r_3 fitted values (*cfr.* table S-IV-S-V) also display slight fluctuation around the refined c-axes. The comparison of the high-resolution XRPD results with the EXAFS analysis can offer a picture of the overall structure at long and short ranges. On the one hand, the calculated uniaxial microstrains, in first approximation originating from the TMs-sublattice, are limited to very low values, effecting only the 3^{rd} or 4^{th} figures in the lattice parameters. On the other hand, the EXAFS first-shell distances display variations of at least an order of magnitude higher than the average lattice. As such, the TM-sublattice appears less prone to accommodate internal strains in the out-of-plane direction as compared to the B-sublattice. The latter, whilst chemically homogeneous, experiences local distortions (*i.e.* structural disorder) but with a much lower effect on entropy than the chemical variations occurring on the TM-layer. This is in fair agreement with DFT results obtained by Feltrin *et al.* on $(Ti_{0.25}Zr_{0.25}Hf_{0.25}V_{0.25})B_2$ [37]. These distortions were enhanced in proximity of particular metals. Titanium and tungsten, for example, act as centers of contraction for the neighbouring borons, while zirconium shows an opposite

effect. Building upon these considerations, the non-perfect 2D arrangement of the B-layers will inevitably impact on the electronic and vibrational bands of the solid, with the potential of altering the electrical, mechanical, and thermal properties, compared to single-element diborides.

3.1. Further insights and outlook

This study highlighted three interesting consequences of the high-entropy effect on boride ceramics: 1. the short-range structure differs from the average one, at least for the first-shell and the B-sublattice; 2. formation of homogeneous and equimolar solid solutions is possible; and 3. the simultaneous substitution of different metals in one sublattice has direct impact on the local structure of both sublattices. While all these points have been the subject of speculation, the complementary information offered by high-resolution XRPD and EXAFS techniques allowed us to address them comprehensively. In particular, the second aspect appears to be deeply dependent on the designed composition and processing history, as observed for example in the case of samples containing W (see Supporting Information). Additionally, the third observation implies that the local order is an implicit function of the average structure, and *vice versa*. As such, while a different combination of TMs influences the average structure (*i.e.* cell parameters), at the same time and for the same TMs the local structure is also modified from the one relative to another combination, following a linear trend (*cfr.* Fig. 2). The enhanced complexity of these systems depends not only on the different masses or atomic-sizes, but also on other parameters such as valence electron concentration (VEC), mixing entropy (ΔS_{mix}), or electronegativity. In our investigation, when more than 4 different TMs occupy the *1a* site (*i.e.* samples X-7, X-8, and X-9), the linear trend observed for the strains in Ti and Zr is lost. However, the comparison between $r_{1,i}$ (for Ti and Zr) and r_1^{sf} using equation 5 can offer an explanation, highlighting a strong correlation between $\epsilon_{1,Ti}$ and $\epsilon_{1,Zr}$ as long as $\epsilon_{1,Ti}^{sf} + \epsilon_{1,Zr}^{sf}$ prevails over the sum of the remaining $\epsilon_{1,i}^{sf}$ with $i \neq$Ti,Zr (*cfr.* Fig. 6). Gu *et al.* performed an extensive computational study on a large series of binary and ternary TM diborides [38] sustaining that a VEC-based descriptor is capable of capturing the overall properties. At the same time, the relative electronegativity, among the constituents of the compounds, also plays a crucial role in capturing the effects of relative charge redistribution (even in separate compounds with the same overall VEC) and therefore in determining property trends. Sangiovanni *et al.* recently proposed an approach for realizing HE refractory

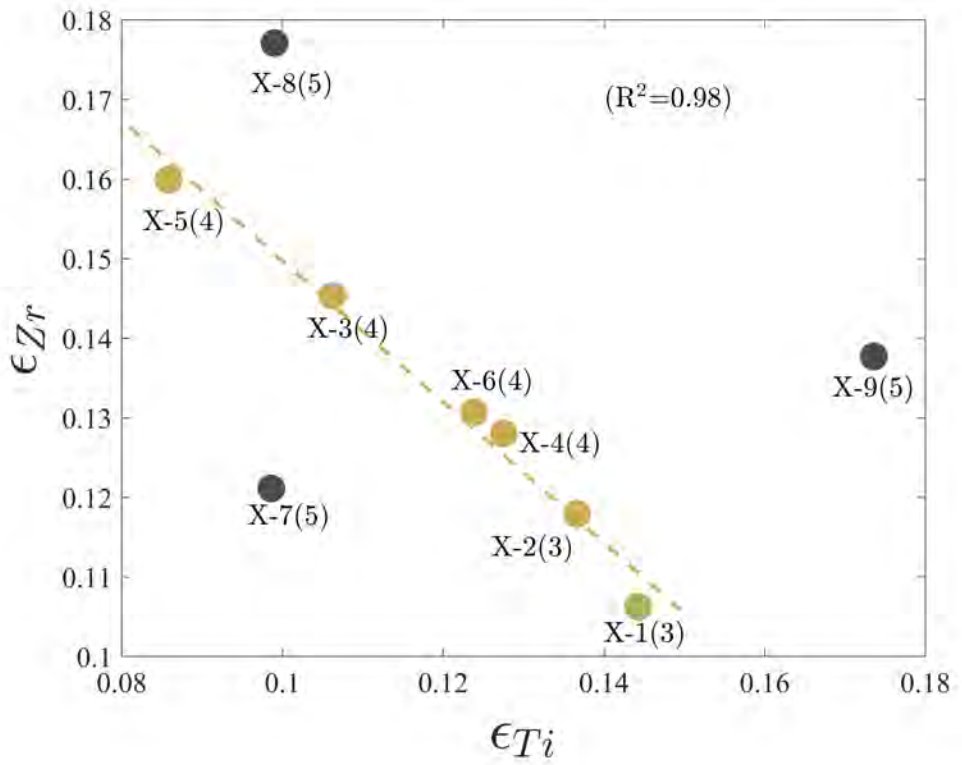

Figure 5: ϵ_{Ti} and ϵ_{Zr} as calculated using equation 4. Relative number of metals is reported between parentheses for each composition. Displayed correlation index R^2 is relative to ϵ_i values with only 3 and 4 TMs (highlighted in orange).

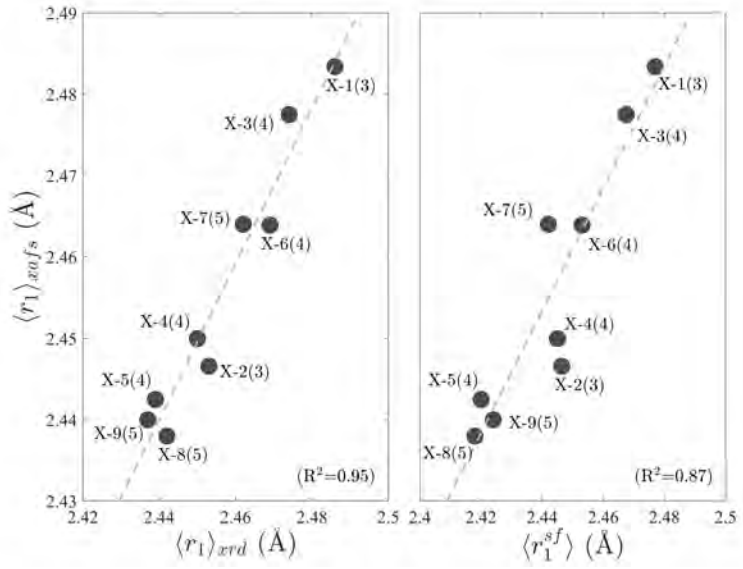

Figure 6: Linear dependence of the average r_1 parameter as calculated from EXAFS (*i.e.* $\langle r_1 \rangle_{xafs}$), diffraction (*i.e.* $\langle r_1 \rangle_{xrd}$), and "strain-free" (*i.e.* $\langle r_1 \rangle_{sf}$). Relative number of metals is reported between parentheses for each composition.

carbides with unique combination of hardness and fracture resistance at high temperature via tailoring the VEC [39]. Among several properties, hardness can be used as benchmark to shed more light between the complexity of a systems and their properties. In this regard, Feng *et al.* [40] along with other authors [41, 42, 43] showed that HE diboride ceramics may be a new class of super-hard materials, and even ultra-incompressible [44]. According to Csanadi *et al.*, the generally observed enhanced hardness obtained from the rule-of-mixture, may be explained through the well-established solid solution strengthening theory [45]. Hardness is affected by many factors, including different slip systems and cross-slip which govern the plastic deformation and therefore the resulting hardness. Hence, whether the local strains arising from random and homogeneous but complex multi-element systems, not necessarily equimolar, can manifest at the bulk scale through measurable effects is a matter of open discussion. The increase in chemical disorder (*i.e.*, increased ΔS_{mix}) may change the dominant slip systems, thereby resulting in variation of ductility and hardness. Mass and size disorder acting as an impedance and scattering the energy of dislocation groups was also

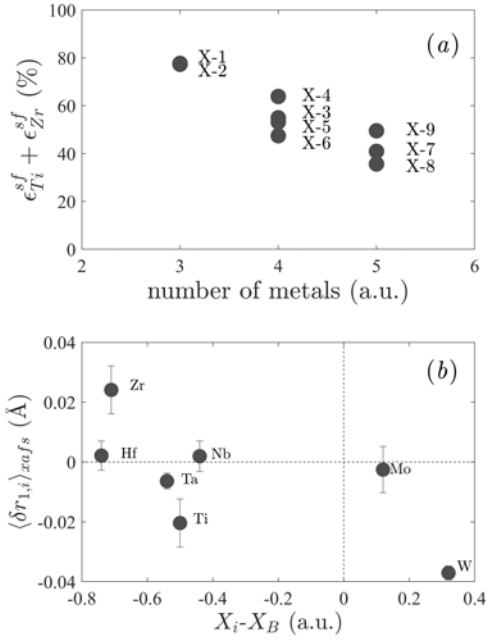

Figure 7: (a) Chart of Ti and Zr "strain-free" ratio (expressed as $\epsilon^{sf}_{Ti}+\epsilon^{sf}_{Ti}$) decreasing with the diboride complexity and reaching lower values when W and Mo are being employed. (b) Relation between the average calculated displacement (δr; standard deviation as error-bars) and calculated electronegativity variation for each transition metal.

suggested by Sarker *et al.* for the HE carbides [46]. The so-called "entropic" strengthening effect has been considered by Dippo *et al.* [47]: whereby different elements with varying sizes induce local strain in the lattice that may impede dislocation nucleation and/or motion. Zhao *et al.* commented on the importance of lattice strain on hardness [36]: they showed that TM-B bonds in W-substituted Mo diborides is strengthened by increasing electron charge transfer from W to Mo. In addition, the same authors suggested that local symmetry reduction is another key factor to hinder dislocation movement for hardness enhancement independent of charge redistribution and VEC variations. This is in agreement with recent study in HE metal diborides where it was demonstrated that incorporating softer WB_2 and MoB_2 made the resulting single phase HE diborides harder [43]. Such a conclusion confirms once again that unusual, unexpected, and often counter-intuitive phenomena can occur. In fact, if the enhanced complexity provided by the

simultaneous presence of several elements was beneficial for achieving higher hardness, any attempt to dissolve an increasingly larger number of differing cations in the same stabilized structure could lead to harder and harder materials. However, when dealing with a property such as hardness, not only the solid solution strengthening and charge redistribution, but also local strains must be considered to fully explain the increase in hardness that have been reported to occur in the wider class of HE borides (which do not exclusively have AlB_2-type structures) [48, 49, 50, 51]. The study of the local structure becomes relevant in this regard, since it may be key to understanding of properties for which local strains have major influence. In the case at hand, the introduction of elements like W and/or Mo gave rise to deviations from the ideal rule-of-mixture model in real solid solutions. A further insight might be offered by Fig. 7*(b)*, showing the EXAFS-calculated average deviation from $r_{1,i}$ (*i.e.* $\langle \delta r_{1,i} \rangle_{xafs}$) with respect to the difference in electronegativity between the relative TM and boron. Metals found on the top side of the graph ($\langle \delta r_{1,i} \rangle_{xafs} > 0$) would exert a negative "chemical pressure" (or "internal pressure") on the B-sublattice (*i.e.*, expanding the planes). In contrast, metals with negative values of $\langle \delta r_{1,i} \rangle_{xafs}$ can be described as having a positive "chemical pressure" effect. While Zr and Ti clearly show an opposite trend of "internal pressure", with other atoms (*i.e.* Hf, Ta, Nb) displaying a milder attitude, they all have lower electronegativity than boron. Clearly, W and Mo, appearing at the bottom-right side of the graph, might be expected to lead to major deviations from properties predicted with rule-of-mixture calculations.

4. Conclusions

Synchrotron based techniques were applied to HEMs to investigate the existence and magnitude of strains arising from the gradual convergence of an increasing number of differing species forced to share and accommodate a new local environment. Contrary to expectations based on rule-of-mixture calculations, the local structure probed by EXAFS analysis in HE-DSS's clearly differs from the average structure measured by long-range techniques (*i.e.* XRPD), with larger deviations occurring for Zr, Ti, and W. When focusing on the 1^{st} *d*-metal-to-boron shell, a different combination of transition metals produces variations at the long range (*i.e.* cell-parameter), for a selected metal, and also changes the local structure from one combination to another, following a linear trend. Nevertheless, the ranking of calculated

distances are in line with that expected on the basis of the metallic radii of the different metals. As a result of the above, we can surmise that not only the local structure affects the long-range order but also the opposite seems to happen, regardless the number and type of metals, which ultimately denote an intimate interconnection between both levels of order.

Acknowledgments

We are grateful to Elettra-Sincrotrone Trieste for providing beamtime and financial support for the XRPD and EXAFS experiments (proposals nr. 20200101 and 20200077). The authors thank A. Sangiorgi (ISTEC-CNR) for assistance in the high-temperature syntheses. The effort of L. Feng, W. Fahrenholtz and G. Hilmas was supported by the U.S. National Science Foundation through grant CMMI-1902069.

Appendix A. XAFS

The EXAFS oscillation can be modelled using the equation:

$$\chi(k) \sim {S_0}^2 \sum_j N_j \frac{|f_j(k)|^2}{k{r_j}^2} \sin(2kr_j + \phi_j(k)) exp(-2\sigma_j^2 k^2) \tag{A.1}$$

where S_0^2 is the amplitude reduction factor, N_j is the path degeneracy of the j-th path, ${\sigma_j}^2$ the mean square displacement, $f_j(k)$ the scattering amplitude, r_j the scattering path distance, and $\phi_j(k)$ the phase-shift. Let us consider the first three single-scattering paths in a random n-elements AlB_2-type lattice (*cfr.* Fig.1). While the first shell is always coordinated by 12 boron atoms; the second shell (N=6 in a mono-atomic diboride) should be split in $\binom{n}{2} + n$ non-degenerate contributions, each one with N=$^6/_n$. The 3^{rd} shell (N=2 in a mono-atomic diboride) will give us the same number of contributions with degeneracy of N=$^2/_n$. While N_j and $f_j(k)$ are fixed for a determined path, for a sample made of n transition metals (thus n EXAFS spectra to analyse) we can count a minimum of $2n$ parameters (*i.e.* one S_0^2-amplitude factor and one E_0-shift for each edge), plus n distances for the 1^{st} shell (central metal coordinated to 12 borons), 3 mean square displacements (one for each shell, assuming negligible differences between different transition metals), and $\binom{n}{2} + n$ mixed r_j-distances for the 2^{nd} and 3^{rd} shells.
Due to the exponential increase in parameters with the number of d-metals,

few approximations were taken into account and the whole fitting procedure is described in the following, with the purpose of fitting the best parameters for the 1^{st} shell (hereafter r_1). The first approximation involves the mean square displacements relative to the first shell (M-B), assumed to be the same for all metals in the same chemical mixture. We also considered a single thermal displacement parameter for the paths relative to the 2^{nd} and 3^{rd} shells (*i.e.* $\sigma_2 = \sigma_3$, yet different from that of the 1^{st} shell, σ_1). Due to the marginal amplitude resulting from the third-shell scattering paths (compared to that of the first two), their contributions were parametrized in order to fit all paths with a single parameter, α, such that $r_3^{ij} = \alpha r_2^{ij}$, where i and j being the indexes relative to the path generated by M_i-M_j. The double scattering paths resulting from the interaction of the central TM-atom with the first-to-first and first-to-second neighbour borons (forming respectively an acute and obtuse triangle) produce a feeble and broad amplitude in the region 2-3.8 Å which were considered negligible and thus neglected from the fitting procedure. Metallic and covalent distances were calculated for all possible combinations of atoms in the AlB_2-type structure and used as reference for the assessment of the 2^{nd} and 3^{rd} shells distance parameters (r_2 and r_3) during the refinement steps. To reduce correlations in the first stages of refinement, r_2 was constrained in groups based on the calculated values (for example, the distances calculated for the pairs Zr-Ta, Zr-Nb, and Ti-Hf share the same value of r_2). After reaching a reasonable fitting for the base parameters, *i.e.* S_0^2, E_0, σ_1, and r_1; the r_2 constraints were lifted in order to improve their values and the overall fitting of r_1. In few cases (*i.e.*, when M^i-M^j distances were highly correlated due to similar values) it was considered reasonable to keep the constraints on r_2^{ij}.

References

[1] T. Chen, T. Shun, J. Yeh, M. Wong, Nanostructured nitride films of multi-element high-entropy alloys by reactive DC sputtering, Surface and Coatings Technology 188-189 (2004) 193–200. doi:10.1016/j.surfcoat.2004.08.023.
URL https://linkinghub.elsevier.com/retrieve/pii/S0257897204006577

[2] C.-Y. Hsu, J.-W. Yeh, S.-K. Chen, T.-T. Shun, Wear resistance and high-temperature compression strength of Fcc CuCoNiCrAl0.5Fe alloy

with boron addition, Metallurgical and Materials Transactions A 35 (5) (2004) 1465–1469. doi:10.1007/s11661-004-0254-x.
URL http://link.springer.com/10.1007/s11661-004-0254-x

[3] P.-K. Huang, J.-W. Yeh, T.-T. Shun, S.-K. Chen, Multi-Principal-Element Alloys with Improved Oxidation and Wear Resistance for Thermal Spray Coating, Advanced Engineering Materials 6 (12) (2004) 74–78. doi:10.1002/adem.200300507.
URL https://onlinelibrary.wiley.com/doi/10.1002/adem.200300507

[4] J.-W. Yeh, S.-J. Lin, T.-S. Chin, J.-Y. Gan, S.-K. Chen, T.-T. Shun, C.-H. Tsau, S.-Y. Chou, Formation of simple crystal structures in Cu-Co-Ni-Cr-Al-Fe-Ti-V alloys with multiprincipal metallic elements, Metallurgical and Materials Transactions A 35 (8) (2004) 2533–2536. doi:10.1007/s11661-006-0234-4.
URL http://link.springer.com/10.1007/s11661-006-0234-4

[5] J.-W. Yeh, S.-K. Chen, S.-J. Lin, J.-Y. Gan, T.-S. Chin, T.-T. Shun, C.-H. Tsau, S.-Y. Chang, Nanostructured High-Entropy Alloys with Multiple Principal Elements: Novel Alloy Design Concepts and Outcomes, Advanced Engineering Materials 6 (5) (2004) 299–303. doi:10.1002/adem.200300567.
URL https://onlinelibrary.wiley.com/doi/10.1002/adem.200300567

[6] J. M. Schneider, How high is the entropy in high entropy ceramics?, Journal of Applied Physics 130 (15) (2021) 150903. doi:10.1063/5.0062523.

[7] A. Kirnbauer, A. Wagner, V. Moraes, D. Primetzhofer, M. Hans, J. Schneider, P. Polcik, P. Mayrhofer, Thermal stability and mechanical properties of sputtered (Hf,Ta,V,W,Zr)-diborides, Acta Materialia 200 (2020) 559–569. doi:10.1016/j.actamat.2020.09.018.
URL https://linkinghub.elsevier.com/retrieve/pii/S1359645420307126

[8] D. Miracle, O. Senkov, A critical review of high entropy alloys and related concepts, Acta Materialia 122 (2017) 448–511. doi:10.1016/j.actamat.2016.08.081.

URL https://linkinghub.elsevier.com/retrieve/pii/S1359645416306759

[9] W.-Y. Huo, S.-Q. Wang, W.-H. Zhu, Z.-L. Zhang, F. Fang, Z.-H. Xie, J.-Q. Jiang, Recent progress on high-entropy materials for electrocatalytic water splitting applications, Tungsten 3 (2) (2021) 161–180. doi:10.1007/s42864-021-00084-8.
URL https://link.springer.com/10.1007/s42864-021-00084-8

[10] A. Sarkar, L. Velasco, D. Wang, Q. Wang, G. Talasila, L. de Biasi, C. Kübel, T. Brezesinski, S. S. Bhattacharya, H. Hahn, B. Breitung, High entropy oxides for reversible energy storage, Nature Communications 9 (1) (2018) 3400. doi:10.1038/s41467-018-05774-5.
URL http://dx.doi.org/10.1038/s41467-018-05774-5http://www.nature.com/articles/s41467-018-05774-5

[11] R.-Z. Zhang, M. J. Reece, Review of high entropy ceramics: design, synthesis, structure and properties, Journal of Materials Chemistry A 7 (39) (2019) 22148–22162. doi:10.1039/C9TA05698J.
URL http://xlink.rsc.org/?DOI=C9TA05698J

[12] F. Z. Dai, Y. Zhou, W. Sun, Segregation of solute atoms (Y, Nb, Ta, Mo and W) in ZrB2 grain boundaries and their effects on grain boundary strengths: A first-principles investigation, Acta Materialia 127 (2017) 312–318. doi:10.1016/j.actamat.2017.01.048.
URL http://dx.doi.org/10.1016/j.actamat.2017.01.048

[13] F. Z. Dai, Y. Sun, B. Wen, H. Xiang, Y. Zhou, Temperature Dependent Thermal and Elastic Properties of High Entropy (Ti0.2Zr0.2Hf0.2Nb0.2Ta0.2)B2: Molecular Dynamics Simulation by Deep Learning Potential, Journal of Materials Science and Technology 72 (2021) 8–15. doi:10.1016/j.jmst.2020.07.014.
URL https://doi.org/10.1016/j.jmst.2020.07.014

[14] F. Monteverde, F. Saraga, M. Gaboardi, L. Feng, G. Hilmas, W. Fahrenholtz, Quantitative inspection of grain-scale chemical inhomogeneities in high-entropy AlB 2 -type transition metal diborides, Journal of the American Ceramic Society (April) (2022) 1–14. doi:10.1111/jace.18619.
URL https://onlinelibrary.wiley.com/doi/10.1111/jace.18619

[15] C. M. Rost, E. Sachet, T. Borman, A. Moballegh, E. C. Dickey, D. Hou, J. L. Jones, S. Curtarolo, J.-P. Maria, Entropy-stabilized oxides, Nature Communications 6 (1) (2015) 8485. doi:10.1038/ncomms9485.
URL http://www.nature.com/articles/ncomms9485

[16] C. M. Rost, Z. Rak, D. W. Brenner, J. Maria, Local structure of the Mg x Ni x Co x Cu x Zn x O(x =0.2) entropy-stabilized oxide: An EXAFS study, Journal of the American Ceramic Society 100 (6) (2017) 2732–2738. doi:10.1111/jace.14756.
URL https://onlinelibrary.wiley.com/doi/10.1111/jace.14756

[17] M. Fracchia, M. Manzoli, U. Anselmi-Tamburini, P. Ghigna, A new eight-cation inverse high entropy spinel with large configurational entropy in both tetrahedral and octahedral sites: Synthesis and cation distribution by X-ray absorption spectroscopy, Scripta Materialia 188 (2020) 26–31. doi:10.1016/j.scriptamat.2020.07.002.
URL https://doi.org/10.1016/j.scriptamat.2020.07.002https://linkinghub.elsevier.com/retrieve/pii/S1359646220304413

[18] B. Jiang, Y. Yu, J. Cui, X. Liu, L. Xie, J. Liao, Q. Zhang, Y. Huang, S. Ning, B. Jia, B. Zhu, S. Bai, L. Chen, S. J. Pennycook, J. He, High-entropy-stabilized chalcogenides with high thermoelectric performance, Science 371 (6531) (2021) 830–834. doi:10.1126/science.abe1292.
URL https://www.science.org/doi/10.1126/science.abe1292

[19] M. R. Chellali, A. Sarkar, S. H. Nandam, S. S. Bhattacharya, B. Breitung, H. Hahn, L. Velasco, On the homogeneity of high entropy oxides: An investigation at the atomic scale, Scripta Materialia 166 (2019) 58–63. doi:10.1016/j.scriptamat.2019.02.039.
URL https://doi.org/10.1016/j.scriptamat.2019.02.039https://linkinghub.elsevier.com/retrieve/pii/S1359646219301253

[20] B. Cheng, H. Lou, A. Sarkar, Z. Zeng, F. Zhang, X. Chen, L. Tan, V. Prakapenka, E. Greenberg, J. Wen, R. Djenadic, H. Hahn, Q. Zeng, Pressure-induced tuning of lattice distortion in a high-entropy oxide, Communications Chemistry 2 (1) (2019) 114. doi:10.1038/s42004-019-0216-2.
URL http://dx.doi.org/10.1038/s42004-019-0216-2http://www.nature.com/articles/s42004-019-0216-2

[21] J. Gild, Y. Zhang, T. Harrington, S. Jiang, T. Hu, M. C. Quinn, W. M. Mellor, N. Zhou, K. Vecchio, J. Luo, High-Entropy Metal Diborides: A New Class of High-Entropy Materials and a New Type of Ultrahigh Temperature Ceramics, Scientific Reports 6 (1) (2016) 37946. doi:10.1038/srep37946.
URL http://www.nature.com/articles/srep37946

[22] J. Gu, J. Zou, S.-K. Sun, H. Wang, S.-Y. Yu, J. Zhang, W. Wang, Z. Fu, Dense and pure high-entropy metal diboride ceramics sintered from self-synthesized powders via boro/carbothermal reduction approach, Science China Materials 62 (12) (2019) 1898–1909. doi:10.1007/s40843-019-9469-4.
URL http://link.springer.com/10.1007/s40843-019-9469-4

[23] Y. Zhang, Z. B. Jiang, S. K. Sun, W. M. Guo, Q. S. Chen, J. X. Qiu, K. Plucknett, H. T. Lin, Microstructure and mechanical properties of high-entropy borides derived from boro/carbothermal reduction, Journal of the European Ceramic Society (2019). doi:10.1016/j.jeurceramsoc.2019.05.017.

[24] F. Monteverde, F. Saraga, Entropy stabilized single-phase (Hf,Nb,Ta,Ti,Zr)B2 solid solution powders obtained via carbo/borothermal reduction, Journal of Alloys and Compounds 824 (2020) 153930. doi:10.1016/j.jallcom.2020.153930.
URL https://linkinghub.elsevier.com/retrieve/pii/S0925838820302930

[25] S. Barbarossa, R. Orrù, V. Cannillo, A. Iacomini, S. Garroni, M. Murgia, G. Cao, Fabrication and Characterization of Quinary High Entropy-Ultra-High Temperature Diborides, Ceramics 4 (2) (2021) 108–120. doi:10.3390/ceramics4020010.
URL https://www.mdpi.com/2571-6131/4/2/10

[26] L. Feng, W. G. Fahrenholtz, G. E. Hilmas, F. Monteverde, Effect of Nb content on the phase composition, densification, microstructure, and mechanical properties of high-entropy boride ceramics, Journal of the European Ceramic Society 41 (1) (2021) 92–100. doi:10.1016/j.jeurceramsoc.2020.08.058.

[27] M. Matas, A. Farhadizadeh, J. Houska, Vacancies and substitutional defects in multicomponent diboride Ti 0.25 Zr 0.25 Hf 0.25 Ta 0.25 B 2 : first-principle study, Journal of Physics: Condensed Matter 34 (9) (2022) 095901. doi:10.1088/1361-648X/ac3db4.
URL https://doi.org/10.1088/1361-648X/ac3db4https://iopscience.iop.org/article/10.1088/1361-648X/ac3db4

[28] L. Feng, W. G. Fahrenholtz, G. E. Hilmas, Two-step synthesis process for high-entropy diboride powders, Journal of the American Ceramic Society 103 (2) (2020) 724–730. doi:10.1111/jace.16801.
URL https://onlinelibrary.wiley.com/doi/10.1111/jace.16801

[29] B. H. Toby, R. B. Von Dreele, GSAS-II: The genesis of a modern open-source all purpose crystallography software package, Journal of Applied Crystallography 46 (2) (2013) 544–549. doi:10.1107/S0021889813003531.

[30] A. Di Cicco, G. Aquilanti, M. Minicucci, E. Principi, N. Novello, A. Cognigni, L. Olivi, Novel xafs capabilities at elettra synchrotron light source, Journal of Physics: Conference Series 190 (4) (2009) 012043. doi:10.1088/1742-6596/190/1/012043.

[31] B. Ravel, M. Newville, ATHENA , ARTEMIS , HEPHAESTUS : data analysis for X-ray absorption spectroscopy using IFEFFIT, Journal of Synchrotron Radiation 12 (4) (2005) 537–541. doi:10.1107/S0909049505012719.
URL http://scripts.iucr.org/cgi-bin/paper?S0909049505012719

[32] F. Monteverde, F. Saraga, M. Gaboardi, J. R. Plaisier, Compositional pathways and anisotropic thermal expansion of high-entropy transition metal diborides, Journal of the European Ceramic Society 41 (13) (2021) 6255–6266. doi:10.1016/j.jeurceramsoc.2021.05.053.
URL https://doi.org/10.1016/j.jeurceramsoc.2021.05.053https://linkinghub.elsevier.com/retrieve/pii/S0955221921003915

[33] Y. Zhou, J. Wang, Z. Li, X. Zhan, J. Wang, First-Principles Investigation on the Chemical Bonding and Intrinsic Elastic Properties of Transition Metal Diborides TMB 2 (TM=Zr, Hf, Nb, Ta, and Y), in:

Ultra-High Temperature Ceramics, John Wiley & Sons, Inc, Hoboken, NJ, 2014, Ch. 4, pp. 60–82. doi:10.1002/9781118700853.ch4.
URL https://onlinelibrary.wiley.com/doi/10.1002/9781118700853.ch4

[34] B. Lönnberg, Thermal expansion studies on the group IV-VII transition metal diborides, Journal of The Less-Common Metals 141 (1) (1988) 145–156. doi:10.1016/0022-5088(88)90219-6.
URL https://www.sciencedirect.com/science/article/abs/pii/0022508888902196

[35] S. Otani, T. Aizawa, N. Kieda, Solid solution ranges of zirconium diboride with other refractory diborides: HfB2, TiB2, TaB2, NbB2, VB2 and CrB2, Journal of Alloys and Compounds 475 (1-2) (2009) 273–275. doi:10.1016/j.jallcom.2008.08.023.
URL https://linkinghub.elsevier.com/retrieve/pii/S0925838808012887

[36] F. Zhao, Q. Tao, C. You, M. Ye, L. Li, Y. Han, S. Dong, X. Wang, T. Cui, P. Zhu, Enhanced hardness in tungsten–substituted molybdenum diboride solid solutions by local symmetry reduction, Materials Chemistry and Physics 251 (May) (2020) 123188. doi:10.1016/j.matchemphys.2020.123188.
URL https://linkinghub.elsevier.com/retrieve/pii/S0254058420305599

[37] A. C. Feltrin, D. Hedman, F. Akhtar, Transformation of metastable dual-phase (Ti 0.25 V 0.25 Zr 0.25 Hf 0.25)B 2 to stable high-entropy single-phase boride by thermal annealing, Applied Physics Letters 119 (16) (2021) 161905. doi:10.1063/5.0066698.
URL https://aip.scitation.org/doi/10.1063/5.0066698

[38] X. Gu, C. Liu, H. Guo, K. Zhang, C. Chen, Sorting transition-metal diborides: New descriptor for mechanical properties, Acta Materialia 207 (2021). doi:10.1016/j.actamat.2021.116685.

[39] D. G. Sangiovanni, W. Mellor, T. Harrington, K. Kaufmann, K. Vecchio, Enhancing plasticity in high-entropy refractory ceramics via tailoring valence electron concentration, Materials & Design 209 (2021) 109932. arXiv:2102.02455, doi:10.1016/j.matdes.2021.109932.

URL https://linkinghub.elsevier.com/retrieve/pii/S0264127521004858

[40] L. Feng, F. Monteverde, W. G. Fahrenholtz, G. E. Hilmas, Superhard high-entropy AlB2-type diboride ceramics, Scripta Materialia 199 (2021). doi:10.1016/j.scriptamat.2021.113855.

[41] Y. Zhang, W.-M. Guo, Z.-B. Jiang, Q.-Q. Zhu, S.-K. Sun, Y. You, K. Plucknett, H.-T. Lin, Dense high-entropy boride ceramics with ultra-high hardness, Scripta Materialia 164 (2019) 135–139. doi:10.1016/j.scriptamat.2019.01.021.
URL https://linkinghub.elsevier.com/retrieve/pii/S1359646219300387

[42] M. Qin, J. Gild, C. Hu, H. Wang, M. S. B. Hoque, J. L. Braun, T. J. Harrington, P. E. Hopkins, K. S. Vecchio, J. Luo, Dual-phase high-entropy ultra-high temperature ceramics, Journal of the European Ceramic Society 40 (15) (2020) 5037–5050. arXiv:2002.09756, doi:10.1016/j.jeurceramsoc.2020.05.040.
URL https://linkinghub.elsevier.com/retrieve/pii/S0955221920303915

[43] M. Qin, J. Gild, H. Wang, T. Harrington, K. S. Vecchio, J. Luo, Dissolving and stabilizing soft WB2 and MoB2 phases into high-entropy borides via boron-metals reactive sintering to attain higher hardness, Journal of the European Ceramic Society 40 (12) (2020) 4348–4353. arXiv:1912.11743, doi:10.1016/j.jeurceramsoc.2020.03.063.
URL https://linkinghub.elsevier.com/retrieve/pii/S0955221920302442

[44] X. Zhang, W. Li, H. Tian, J. Liu, C. Li, H. Dong, J. Chen, M. Song, B. Chen, H. Sheng, S. Wang, D. Zhang, H. Zhang, Ultra-incompressible High-Entropy Diborides, The Journal of Physical Chemistry Letters 12 (12) (2021) 3106–3113. doi:10.1021/acs.jpclett.1c00399.
URL https://pubs.acs.org/doi/10.1021/acs.jpclett.1c00399

[45] T. Csanádi, E. Castle, M. J. Reece, J. Dusza, Strength enhancement and slip behaviour of high-entropy carbide grains during microcompression, Scientific Reports 9 (1) (2019) 10200. doi:10.1038/

s41598-019-46614-w.
URL http://www.nature.com/articles/s41598-019-46614-w

[46] P. Sarker, T. Harrington, C. Toher, C. Oses, M. Samiee, J.-P. Maria, D. W. Brenner, K. S. Vecchio, S. Curtarolo, High-entropy high-hardness metal carbides discovered by entropy descriptors, Nature Communications 9 (1) (2018) 4980. arXiv:1811.07730, doi:10.1038/s41467-018-07160-7.
URL http://dx.doi.org/10.1038/s41467-018-07160-7http://www.nature.com/articles/s41467-018-07160-7

[47] O. F. Dippo, N. Mesgarzadeh, T. J. Harrington, G. D. Schrader, K. S. Vecchio, Bulk high-entropy nitrides and carbonitrides, Scientific Reports 10 (1) (2020) 21288. doi:10.1038/s41598-020-78175-8.
URL https://doi.org/10.1038/s41598-020-78175-8http://www.nature.com/articles/s41598-020-78175-8

[48] L. E. Pangilinan, C. L. Turner, G. Akopov, M. Anderson, R. Mohammadi, R. B. Kaner, Superhard Tungsten Diboride-Based Solid Solutions, Inorganic Chemistry 57 (24) (2018) 15305–15313. doi:10.1021/acs.inorgchem.8b02620.
URL https://pubs.acs.org/doi/10.1021/acs.inorgchem.8b02620

[49] L. E. Pangilinan, S. Hu, S. G. Hamilton, S. H. Tolbert, R. B. Kaner, Hardening Effects in Superhard Transition-Metal Borides, Accounts of Materials Research 3 (1) (2022) 100–109. doi:10.1021/accountsmr.1c00192.
URL https://pubs.acs.org/doi/10.1021/accountsmr.1c00192

[50] G. Akopov, L. E. Pangilinan, R. Mohammadi, R. B. Kaner, Perspective: Superhard metal borides: A look forward, APL Materials 6 (7) (2018) 070901. doi:10.1063/1.5040763.
URL http://dx.doi.org/10.1063/1.5040763http://aip.scitation.org/doi/10.1063/1.5040763

[51] M. Qin, Q. Yan, H. Wang, C. Hu, K. S. Vecchio, J. Luo, High-entropy monoborides: Towards superhard materials, Scripta Materialia 189 (2020) 101–105. doi:10.1016/j.scriptamat.2020.08.018.
URL https://doi.org/10.1016/j.scriptamat.2020.08.018https://linkinghub.elsevier.com/retrieve/pii/S1359646220305443

SUPPLEMENTARY INFORMATION

XRPD refinements

Table S-I: Summary of the XRPD-refined lattice parameters, weighted profile factor, goodness of fit (*gof*), and equatorial and axial microstrain.

ID	composition	a(Å)	c(Å)	R_{wp}(%)	*gof*	$(\frac{\Delta d}{d})_{eq}$(%)	$(\frac{\Delta d}{d})_{ax}$(%)
X-1	TiZrHf	3.116904(33)	3.429609(21)	11.96	1.18	0.04	0.06
X-2	TiZrTa	3.095627(22)	3.359952(51)	26.32	1.14	0.06	0.13
X-3	TiZrHfNb	3.112209(15)	3.400761(10)	9.99	1.83	0.04	0.07
X-4	TiZrNbTa	3.097907(16)	3.349202(10)	8.93	1.69	0.23	0.09
X-5	TiZrMoTa	3.084012(55)	3.332336(33)	22.44	1.15	0	0
X-6	TiZrHfW	3.105021(29)	3.396209(20)	9.84	1.79	0.16	0.09
X-7	TiZrHfNbMo	3.100660(38)	3.380211(26)	22.16	1.31	0.04	0.07
X-8	TiZrHfMoW	3.082547(45)	3.344904(32)	11.17	1.13	0.21	0.60
X-9	TiZrNbMoTa	3.085639(33)	3.326633(23)	17.90	1.65	0.06	0.23

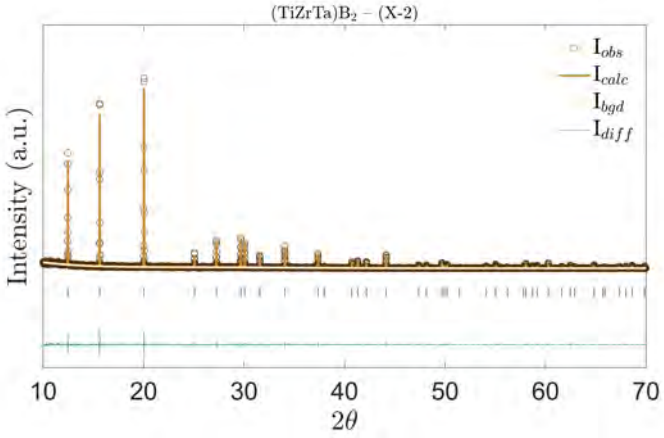

Figure S-1: Rietveld refinement of X-2.

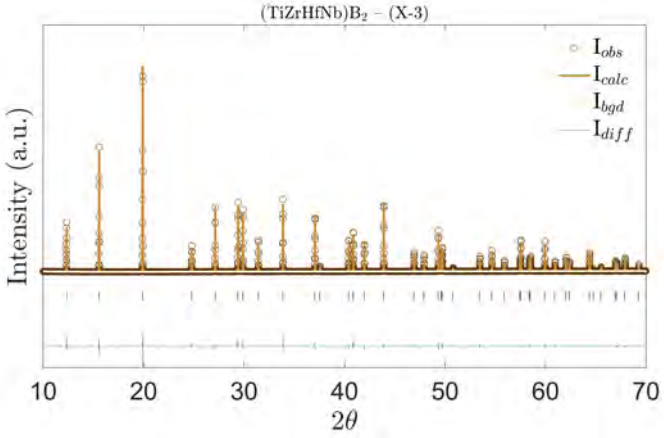

Figure S-2: Rietveld refinement of X-3.

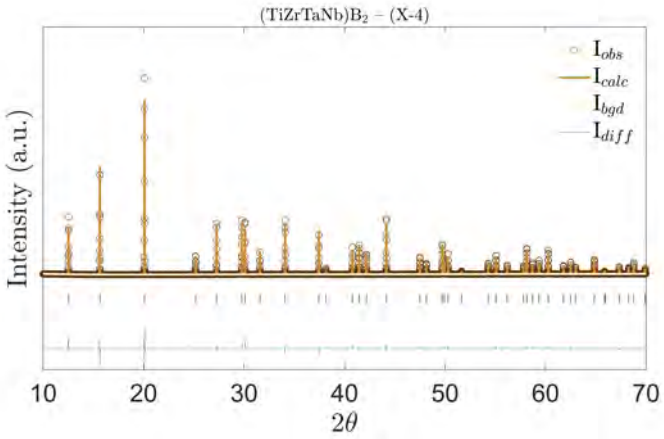

Figure S-3: Rietveld refinement of X-4.

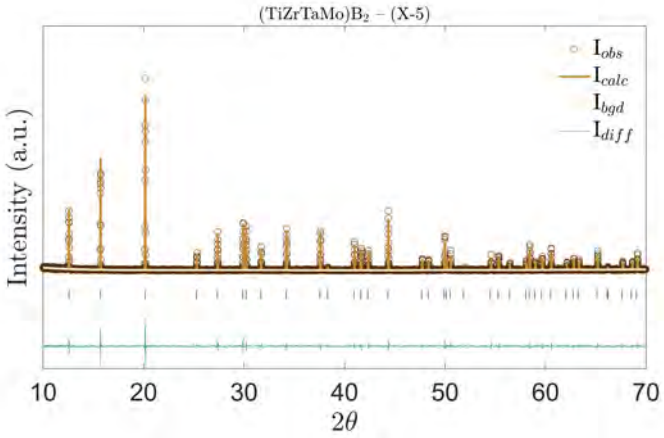

Figure S-4: Rietveld refinement of X-5.

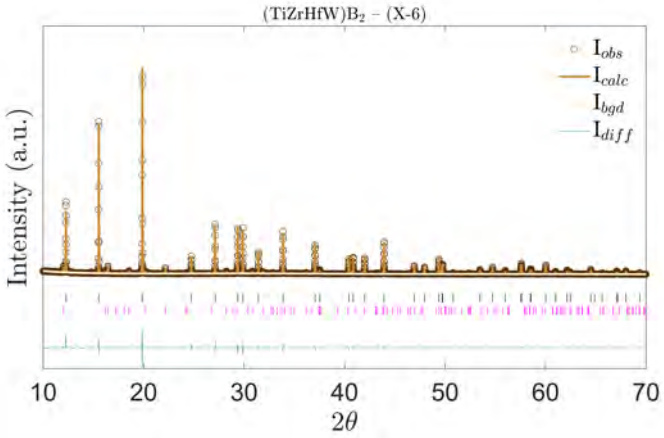

Figure S-5: Rietveld refinement of X-6. The W_2B_5-type impurity phase (s.g. $P6_3/mmc$) is indexed by magenta tickmarks and refined in 4% molar amount assuming the W_2B_5 composition.

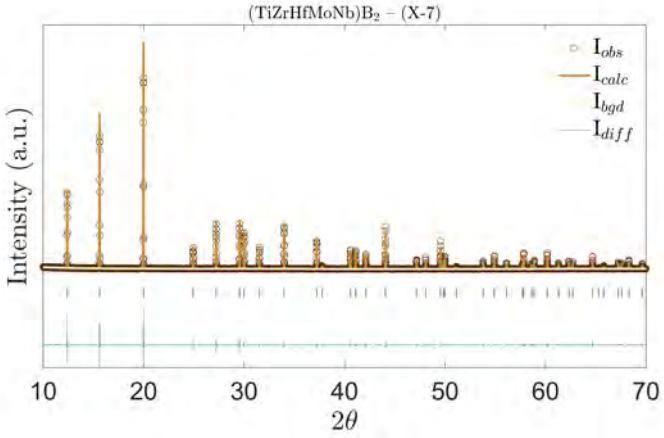

Figure S-6: Rietveld refinement of X-7.

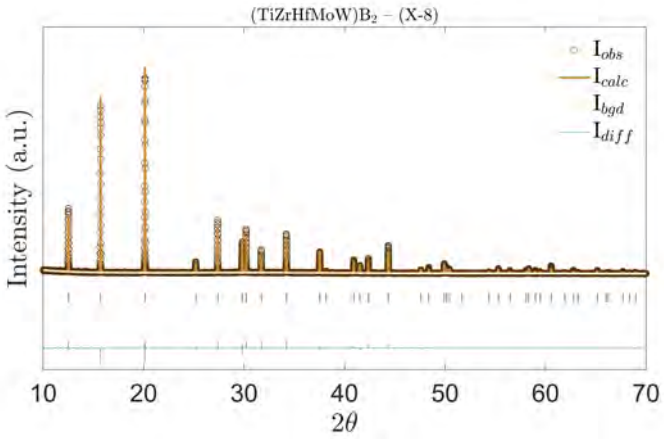

Figure S-7: Rietveld refinement of X-8.

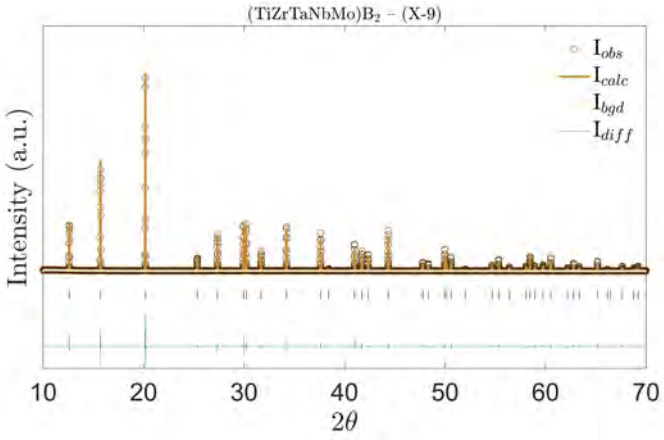

Figure S-8: Rietveld refinement of X-9.

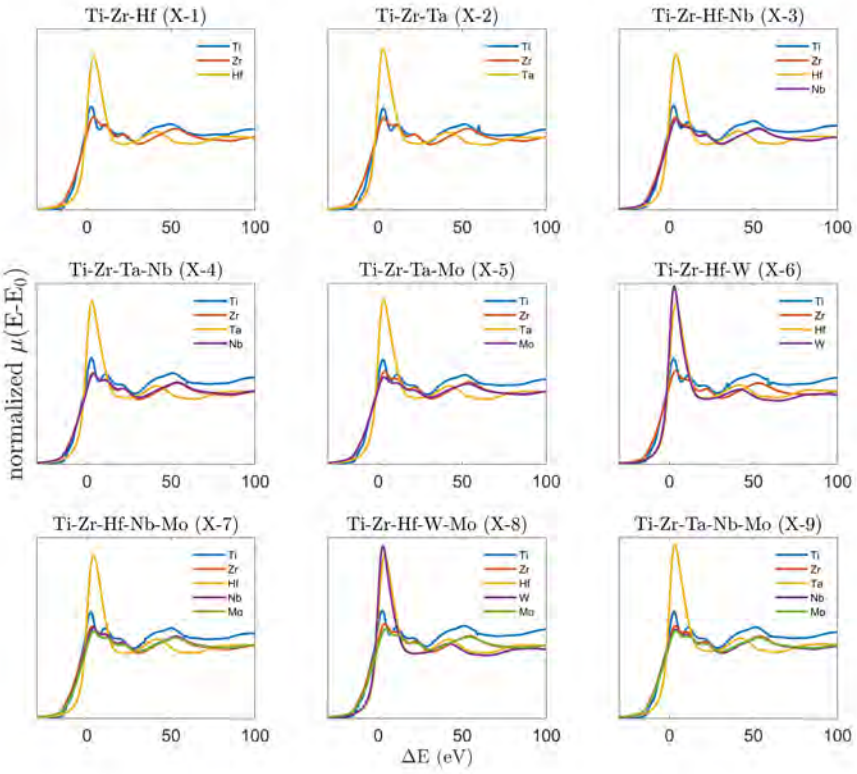

Figure S-9: Normalized and aligned X-ray absorption spectra in the near-edge region.

Inclusions of W_2B_5 in sample X-6 and additional tables

SEM-EDS analysis on a polished section of the as-synthesized sample X-6 identified the main HE diboride matrix and the cited impurity (see Fig. S-10). The former phase is the (TiZrHfW)B_2 solid solution with a W content lower than that expected from the equimolar case. The residual available W remained trapped in this impurity. It is clear that the solubility of W in the compositional system X-6 is limited and an equimolar concentration of W with Ti, Zr, and Hf cannot be achieved. The X-6 composition was object of more attention so that the starting molar content of W was reduced from 25 to 16%: this composition was labeled X-6-1. The X-6-1 sample was processed and analyzed, EXAFS apart, according to the procedures described in Methods: the impurity phase disappeared and a non-equimolar HE diboride was formed (*cfr.* Fig. S-11). In this way the partial solubility of W in the X-6 system was demonstrated. To overcome this limit, the starting X-6-1 combination was revised adding the fifth element Mo to boost the overall mutual solubility. This is actually the genesis of composition X-8. Only for that system, the second step of the synthesis was conducted in mild vacuum (2 Pa) up to 2273 K using the special SPS furnace (mod. DSC10, Thermal Technology) to take full advantage from the application of an extra pressure of 50 MPa. More details are reported elsewhere [28]. This processing variation was very effective to completely dissolve 20 at% W in the only formed nearly-equimolar HE diboride. In Fig. S-12 the nearly homogeneous distribution of various TMs is shown. The weighted average of the TMs contents (normalized to 100%) is (20.1±0.02) at%, meaning that this sample can be considered as an equimolar DSS.

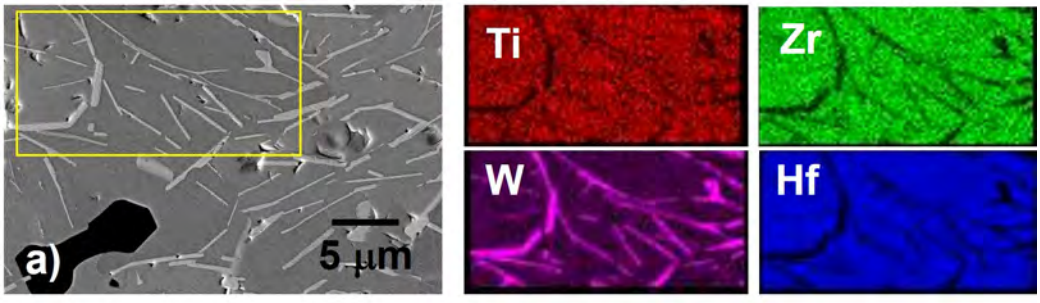

Figure S-10: a) BSE-SEM micrograph from as-synthesized sample X-6 with needle-like bright W-rich impurities. Color maps of the TM distribution are generated from the area within the yellow box in a). The black features in a) comes from unreacted boron carbide.

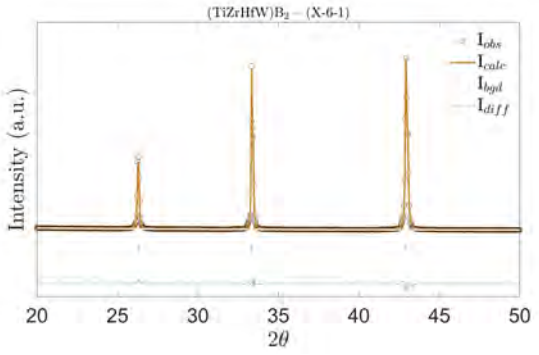

Figure S-11: Laboratory (Cu-K$_\alpha$) XRPD pattern and Rietveld refinement of sample X-6-1. Refined parameters: a=3.10318(17)Å, c=3.39302(13) Å (R$_{wp}$=5.6%, s.g. P6/mmm).

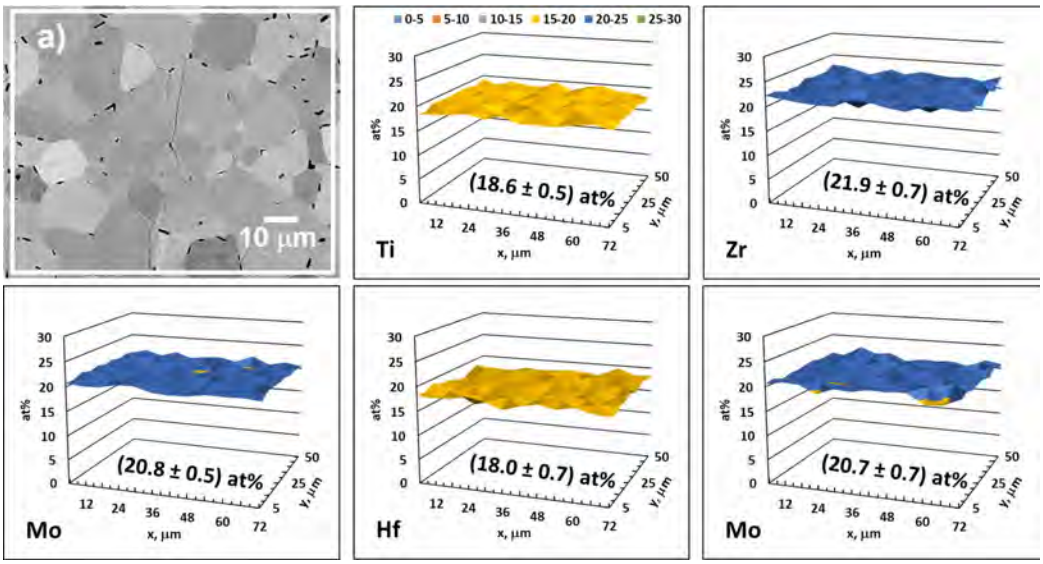

Figure S-12: a) BSE-SEM of the as-synthesized X-8 sample. Quantitative elemental maps of TM acquired inside the 72x50 mm white box: for each TM, mean ±1 standard deviation is indicated. The colored palette in the Ti map is valid for the remaining TMs.

Table S-II: Summary of second-shell distances (M^i-M^j) as refined from EXAFS global fitting (errors between parentheses). Repeated values are omitted for the sake of clarity. Errors for constrained parameters are shown only the first time and then replaced by (-).

ID	composition	Ti−Ti	Ti−Zr	Ti−Hf	Ti−Nb	Ti−Mo	Ti−Ta	Ti−W
X-1	TiZrHf	3.12(02)	3.11(02)	3.12(01)	-	-	-	-
X-2	TiZrTa	3.09(03)	3.09(01)	-	-	-	3.09(01)	-
X-3	TiZrHfNb	3.14(02)	-	3.13(01)	-	-	-	-
X-4	TiZrTaNb	3.11(04)	3.12(02)	-	3.1(02)	-	3.12(01)	-
X-5	TiZrTaMo	3.06(01)	3.07(01)	-	-	3.1(01)	3.1(01)	-
X-6	TiZrHfW	3.1(02)	3.08(02)	3.11(01)	-	-	-	3.09(02)
X-7	TiZrHfNbMo	3.09(04)	3.12(02)	3.11(02)	3.11(02)	3.08(01)	-	-
X-8	TiZrHfMoW	3.11(03)	3.13(02)	3.14(02)	-	3.06(-)	-	3.06(02)
X-9	TiZrTaNbMo	3.02(07)	3.07(04)	-	3.03(04)	3.13(05)	3.09(04)	-
ID	composition	Zr−Ti	Zr−Zr	Zr−Hf	Zr−Nb	Zr−Mo	Zr−Ta	Zr−W
X-1	TiZrHf	-	3.13(02)	3.13(01)	-	-	-	-
X-2	TiZrTa	-	3.1(01)	-	-	-	3.1(01)	-
X-3	TiZrHfNb	3.12(01)	3.13(01)	3.13(01)	-	-	-	-
X-4	TiZrTaNb	-	3.12(03)	-	3.11(03)	-	3.11(01)	-
X-5	TiZrTaMo	-	3.1(01)	-	-	3.09(01)	3.09(01)	-
X-6	TiZrHfW	-	3.11(01)	3.11(01)	-	-	-	3.11(01)
X-7	TiZrHfNbMo	-	3.13(02)	3.11(01)	3.11(-)	3.09(01)	-	-
X-8	TiZrHfMoW	-	3.1(02)	3.09(02)	-	3.13(-)	-	3.13(02)
X-9	TiZrTaNbMo	-	3.12(2)	-	3.1(11)	3.12(16)	3.13(05)	-
ID	composition	Hf−Ti	Hf−Zr	Hf−Hf	Hf−Nb	Hf−Mo	Hf−Ta	Hf−W
X-1	TiZrHf	-	-	3.13(02)	-	-	-	-
X-2	TiZrTa	-	-	-	-	-	-	-
X-3	TiZrHfNb	-	-	3.13(02)	-	-	-	-
X-4	TiZrTaNb	-	-	-	-	-	-	-
X-5	TiZrTaMo	-	-	-	-	-	-	-
X-6	TiZrHfW	-	-	3.12(01)	-	-	-	3.1(01)
X-7	TiZrHfNbMo	-	-	3.11(-)	3.11(01)	3.09(-)	-	-
X-8	TiZrHfMoW	-	-	3.07(03)	-	3.13(-)	-	3.13(02)
X-9	TiZrTaNbMo	-	-	-	-	-	-	-
ID	composition	Nb−Ti	Nb−Zr	Nb−Hf	Nb−Nb	Nb−Mo	Nb−Ta	Nb−W
X-1	TiZrHf	-	-	-	-	-	-	-
X-2	TiZrTa	-	-	-	-	-	-	-
X-3	TiZrHfNb	3.14(01)	3.12(01)	3.12(01)	3.14(01)	-	-	-
X-4	TiZrTaNb	-	-	-	3.1(03)	-	3.12(01)	-
X-5	TiZrTaMo	-	-	-	-	-	-	-
X-6	TiZrHfW	-	-	-	-	-	-	-
X-7	TiZrHfNbMo	-	-	-	3.12(02)	3.08(-)	-	-
X-8	TiZrHfMoW	-	-	-	-	-	-	-
X-9	TiZrTaNbMo	-	-	-	3.04(09)	3.13(1)	-	-

Table S-III: Summary of second-shell distances (M^i-M^j) as refined from EXAFS global fitting (errors between parentheses). Repeated values are omitted for the sake of clarity. Errors for constrained parameters are shown only the first time and then replaced by (-).

ID	composition	Mo−Ti	Mo−Zr	Mo−Hf	Mo−Nb	Mo−Mo	Mo−Ta	Mo−W
X-1	TiZrHf	-	-	-	-	-	-	-
X-2	TiZrTa	-	-	-	-	-	-	-
X-3	TiZrHfNb	-	-	-	-	-	-	-
X-4	TiZrTaNb	-	-	-	-	-	-	-
X-5	TiZrTaMo	-	-	-	-	3.11(01)	3.08(01)	-
X-6	TiZrHfW	-	-	-	-	-	-	-
X-7	TiZrHfNbMo	-	-	-	-	3.15(01)	-	-
X-8	TiZrHfMoW	-	-	-	-	3.04(-)	-	3.04(-)
X-9	TiZrTaNbMo	-	-	-	-	3.1(17)	-	-
ID	composition	Ta−Ti	Ta−Zr	Ta−Hf	Ta−Nb	Ta−Mo	Ta−Ta	Ta−W
X-1	TiZrHf	-	-	-	-	-	-	-
X-2	TiZrTa	-	-	-	-	-	3.1(01)	-
X-3	TiZrHfNb	-	-	-	-	-	-	-
X-4	TiZrTaNb	-	-	-	-	-	3.12(01)	-
X-5	TiZrTaMo	-	-	-	-	-	3.09(01)	-
X-6	TiZrHfW	-	-	-	-	-	-	-
X-7	TiZrHfNbMo	-	-	-	-	-	-	-
X-8	TiZrHfMoW	-	-	-	-	-	-	-
X-9	TiZrTaNbMo	-	-	-	3.07(04)	3.11(05)	3.1(05)	-
ID	composition	W−Ti	W−Zr	W−Hf	W−Nb	W−Mo	W−Ta	W−W
X-1	TiZrHf	-	-	-	-	-	-	-
X-2	TiZrTa	-	-	-	-	-	-	-
X-3	TiZrHfNb	-	-	-	-	-	-	-
X-4	TiZrTaNb	-	-	-	-	-	-	-
X-5	TiZrTaMo	-	-	-	-	-	-	-
X-6	TiZrHfW	-	-	-	-	-	-	3.11(01)
X-7	TiZrHfNbMo	-	-	-	-	-	-	-
X-8	TiZrHfMoW	-	-	-	-	-	-	3.04(04)
X-9	TiZrTaNbMo	-	-	-	-	-	-	-

Table S-IV: Summary of third-shell distances (M^i-M^j) obtained as described in Appendix A from the EXAFS global fitting. Repeated values are omitted for the sake of clarity.

ID	composition	Ti−Ti	Ti−Zr	Ti−Hf	Ti−Nb	Ti−Mo	Ti−Ta	Ti−W
X-1	TiZrHf	3.43	3.43	3.43	-	-	-	-
X-2	TiZrTa	3.27	3.29	-	-	-	3.27	-
X-3	TiZrHfNb	3.5	-	3.48	-	-	-	-
X-4	TiZrTaNb	3.38	3.41	-	3.36	-	3.43	-
X-5	TiZrTaMo	3.18	3.22	-	-	3.42	3.48	-
X-6	TiZrHfW	3.36	3.2	3.4	-	-	-	3.27
X-7	TiZrHfNbMo	3.35	3.44	3.43	3.41	3.3	-	-
X-8	TiZrHfMoW	3.41	3.45	3.47	-	3.31	-	3.31
X-9	TiZrTaNbMo	3.28	3.31	-	3.29	3.36	3.33	-
ID	composition	Zr−Ti	Zr−Zr	Zr−Hf	Zr−Nb	Zr−Mo	Zr−Ta	Zr−W
X-1	TiZrHf	-	3.43	3.44	-	-	-	-
X-2	TiZrTa	-	3.39	-	-	-	3.39	-
X-3	TiZrHfNb	3.45	3.48	3.47	-	-	-	-
X-4	TiZrTaNb	-	3.41	-	3.39	-	3.4	-
X-5	TiZrTaMo	-	3.48	-	-	3.35	3.41	-
X-6	TiZrHfW	-	3.44	3.42	-	-	-	3.45
X-7	TiZrHfNbMo	-	3.48	3.43	3.43	3.36	-	-
X-8	TiZrHfMoW	-	3.39	3.36	-	3.44	-	3.44
X-9	TiZrTaNbMo	-	3.35	-	3.33	3.35	3.36	-
ID	composition	Hf−Ti	Hf−Zr	Hf−Hf	Hf−Nb	Hf−Mo	Hf−Ta	Hf−W
X-1	TiZrHf	-	-	3.44	-	-	-	-
X-2	TiZrTa	-	-	-	-	-	-	-
X-3	TiZrHfNb	-	-	3.49	-	-	-	-
X-4	TiZrTaNb	-	-	-	-	-	-	-
X-5	TiZrTaMo	-	-	-	-	-	-	-
X-6	TiZrHfW	-	-	3.49	-	-	-	3.34
X-7	TiZrHfNbMo	-	-	3.43	3.43	3.36	-	-
X-8	TiZrHfMoW	-	-	3.33	-	3.44	-	3.44
X-9	TiZrTaNbMo	-	-	-	-	-	-	-
ID	composition	Nb−Ti	Nb−Zr	Nb−Hf	Nb−Nb	Nb−Mo	Nb−Ta	Nb−W
X-1	TiZrHf	-	-	-	-	-	-	-
X-2	TiZrTa	-	-	-	-	-	-	-
X-3	TiZrHfNb	3.5	3.42	3.45	3.51	-	-	-
X-4	TiZrTaNb	-	-	-	3.37	-	3.42	-
X-5	TiZrTaMo	-	-	40 -	-	-	-	-
X-6	TiZrHfW	-	-	-	-	-	-	-
X-7	TiZrHfNbMo	-	-	-	3.46	3.3	-	-
X-8	TiZrHfMoW	-	-	-	-	-	-	-
X-9	TiZrTaNbMo	-	-	-	3.29	3.36	-	-

Table S-V: Summary of third-shell distances (M^i-M^j) obtained as described in Appendix A from the EXAFS global fitting. Repeated values are omitted for the sake of clarity.

ID	composition	Mo−Ti	Mo−Zr	Mo−Hf	Mo−Nb	Mo−Mo	Mo−Ta	Mo−W
X-1	TiZrHf	-	-	-	-	-	-	-
X-2	TiZrTa	-	-	-	-	-	-	-
X-3	TiZrHfNb	-	-	-	-	-	-	-
X-4	TiZrTaNb	-	-	-	-	-	-	-
X-5	TiZrTaMo	-	-	-	-	3.51	3.3	-
X-6	TiZrHfW	-	-	-	-	-	-	-
X-7	TiZrHfNbMo	-	-	-	-	3.56	-	-
X-8	TiZrHfMoW	-	-	-	-	3.24	-	3.24
X-9	TiZrTaNbMo	-	-	-	-	3.34	-	-
ID	composition	Ta−Ti	Ta−Zr	Ta−Hf	Ta−Nb	Ta−Mo	Ta−Ta	Ta−W
X-1	TiZrHf	-	-	-	-	-	-	-
X-2	TiZrTa	-	-	-	-	-	3.37	-
X-3	TiZrHfNb	-	-	-	-	-	-	-
X-4	TiZrTaNb	-	-	-	-	-	3.44	-
X-5	TiZrTaMo	-	-	-	-	-	3.34	-
X-6	TiZrHfW	-	-	-	-	-	-	-
X-7	TiZrHfNbMo	-	-	-	-	-	-	-
X-8	TiZrHfMoW	-	-	-	-	-	-	-
X-9	TiZrTaNbMo	-	-	-	3.32	3.34	3.34	-
ID	composition	W−Ti	W−Zr	W−Hf	W−Nb	W−Mo	W−Ta	W−W
X-1	TiZrHf	-	-	-	-	-	-	-
X-2	TiZrTa	-	-	-	-	-	-	-
X-3	TiZrHfNb	-	-	-	-	-	-	-
X-4	TiZrTaNb	-	-	-	-	-	-	-
X-5	TiZrTaMo	-	-	-	-	-	-	-
X-6	TiZrHfW	-	-	-	-	-	-	3.46
X-7	TiZrHfNbMo	-	-	-	-	-	-	-
X-8	TiZrHfMoW	-	-	-	-	-	-	3.24
X-9	TiZrTaNbMo	-	-	-	-	-	-	-

Table S-VI: Atomic radii, hexagonal cell parameters, and calculated "strain-free" 1^{st} shell distances for single phases AlB_2-type (P6/mmm) TM diborides.

	atomic radius(Å)	a(Å)	c(Å)	$\langle r_1 \rangle$	Reference
TiB_2	1.76	3.03	3.24	2.38	[34]
ZrB_2	2.06	3.17	3.53	2.54	[34]
HfB_2	2.08	3.14	3.48	2.51	[34]
NbB_2	1.98	3.1	3.31	2.44	[35]
TaB_2	2.00	3.1	3.25	2.42	[35]
MoB_2	1.90	3.05	3.07	2.34	[36]
WB_2	1.93	3.02	3.05	2.32	[36]